Available online at www.sciencedirect.com
ScienceDirect
Trans. Nonferrous Met. Soc. China 30(2020) 134−146
Transactions of Nonferrous Metals Society of China
www.tnmsc.cn

Hot deformation behavior of Ti−6Al−4V−0.1Ru alloy during isothermal compression

Yu-feng XIA, Wei JIANG, Qian CHENG, Lai JIANG, Li JIN

College of Materials Science and Engineering, Chongqing University, Chongqing 400044, China

Received 13 March 2019; accepted 28 October 2019

Abstract: The hot deformation behavior of Ti−6Al−4V−0.1Ru titanium alloy was investigated by isothermal compression tests on a Gleeble−3500 thermal simulator over deformation temperature range of 1023−1423 K and strain rate of 0.01−10 s^{-1}. Arrhenius-type constitutive models were developed for temperature ranges of both $\alpha+\beta$ dual phase and β single phase at strain of 0.1. Afterwards, a series of material constants (including activation energy Q, material constants n, α and ln A) as polynomial functions of strain were introduced into Arrhenius-type models. Finally, the improved Arrhenius-type models in temperature field of $\alpha+\beta$ and β phase were constructed. The results show that the improved Arrhenius-type models contribute to the calculation of Zener−Hollomon (Z) parameter, and the microstructural evolution mechanism is uncovered by combining microstructure observations with Z-parameter. Furthermore, the improved Arrhenius-type models are also helpful to improve the accuracy of finite element method (FEM) simulation in the deformation process of Ti−6Al−4V−0.1Ru titanium alloy.

Key words: Ti−6Al−4V−0.1Ru titanium alloy; Arrhenius-type constitutive model; Zener−Hollomon parameter; microstructural evolution; FEM simulation

1 Introduction

The typical $\alpha+\beta$ titanium alloy Ti−6Al−4V−0.1Ru is widely used in shipbuilding industry because of excellent mechanical properties such as high specific strength, high corrosion resistance, favorable elastic modulus and low density [1,2]. It is well recognized that the hot deformation behavior of titanium alloy is of great complexity and strongly sensitive to the deformation parameters involving strain rate, temperature, and strain [3]. During hot deformation process, there are various inter-connecting metallurgical phenomena such as work hardening (WH), dynamic recovery (DRV) and dynamic recrystallization (DRX), which control the microstructural evolution and mechanical properties. In the initial stage, working hardening results in increased flow stress of metals and low ductility. With the deformation temperature rising, the appearance of phase transformation induces obvious dynamic softening phenomena like DRX or DRV, which lead to stable plastic flow state and thereby high ductility. Therefore, it is important to understand the hot deformation behavior of alloy for improving the forming quality of hot formed components [4,5]. Meanwhile, the constitutive modeling of flow behavior of alloy has been studied extensively and successfully used to describe the hot deformation behavior of alloy due to the effective role in metallurgical characteristics. On the basis of Voyiadiajis−Abed (VA) model and considering the effect of phase transformation, TABEI et al [6] established a microstructure-based constitutive relation and described the deformation behavior of Ti−6Al−4V alloy. HIROAKI et al [7] focused on a series of microstructural predictions regarding the dynamic recrystallization (DRX)

Foundation item: Projected (51775068) supported by the National Natural Science Foundation of China
Corresponding author: Yu-feng XIA; Tel: +86-23-65111493; E-mail: 201709021063@cqu.edu.cn
DOI: 10.1016/S1003-6326(19)65186-1

behavior and established corresponding constitutive models to enable the reliable prediction of properties of Ti−6Al−4V alloy after forging in the $\alpha+\beta$ region. Compared with other titanium alloys, Ti−6Al−4V−0.1Ru has excellent comprehensive properties in seawater and acidic hydrocarbon compounds, and it has been proven that it has excellent corrosion resistance to chloride ion cracking and stress corrosion [8,9]. However, accurate characterization on the hot deformation behavior of Ti−6Al−4V−0.1Ru for designing hot working processes with correct finite element model of numerical simulation is still limited. Consequently, the deep investigation of the microstructural evolution coupled with flow behavior and appropriate constitutive model is indispensable.

The constitutive model has been widely used to study the relationship between material rheological stress and deformation parameters, which can be mainly divided into phenomenological, physically-based and artificial neural network models [3]. The phenomenological model has nothing to do with physical background but just fits experimental observation and was widely employed for the satisfactory prediction precision. Additionally, the notable feature is that it only needs to calculate the necessary material constants based on limited experimental results and can be easily calibrated by the multivariate nonlinear regression analysis [10]. Simultaneously, some of the important parameters such as the activation energy of deformation (Q) and the Zener−Hollomon parameter (Z) in the model can be used to reveal the mechanism of microstructure evolution [11,12]. As a typical phenomenological model, Arrhenius equation is most widely used to describe the relationship among deformation parameters because its applicability is not constrained by the range of deformation temperature and strain rate. Considering the effect of strain on the flow stress, the improved Arrhenius-type was often constructed to improve model accuracy. MANDAL et al [13] carried out a revised strain-dependent hyperbolic sine constitutive model to predict the high-temperature deformation behaviors of alloy D9. Besides, the improved Arrhenius-type model was extensively used to predict the elevated temperature flow behaviors of alloys, such as as-cast AZ80 [14], Al−Zn−Mg−Er−Zr [15], 42CrMo [16], Ti−6Al−4V [17] and as-cast Ti60 [12]. Therefore, it is necessary to construct improved Arrhenius-type model to characterize the hot deformation behaviors of Ti−6Al−4V−0.1Ru titanium alloy due to its high deformation resistance, wide forming temperature and complex microstructure change.

In this work, true stress−strain data of Ti−6Al−4V−0.1Ru titanium alloy were obtained through the isothermal compression tests in the temperature range of 1023−1423 K and strain rate range of 0.01−10 s^{-1}. The Arrhenius-type constitutive models of $\alpha+\beta$ phase and β phase temperature field were established. Based on the improved Arrhenius-type model, two potential applications were implemented. The Z-parameter maps at the strain of 0.9 were built on $\alpha+\beta$ phase and β single phase temperature field. Combined with microstructure observation with Z-parameter at the strain of 0.9, the Z-parameter maps revealed the microstructural evolution of $\alpha+\beta$ and β phase temperature field. Simultaneously, in order to evaluate the predication performance of the improved Arrhenius-type constitutive model, the flow curves were used to simulate the isothermal compression tests.

2 Experimental

The material employed in the current study is cold-rolled Ti−6Al−4V−0.1Ru titanium alloy which is a kind of $\alpha+\beta$ titanium alloy. The chemical composition (wt.%) of this alloy is as follows: Fe ≤0.25, C ≤0.08, N ≤0.03, H ≤0.015, O ≤0.13, Al 5.5−6.5, V 3.5−4.5, Ru 0.08−0.14 and Ti balanced. The β transus temperature is about 1198 K. The specimen was homogenized at 973 K for 12 h and machined into cylinder with 8 mm in diameter and 12 mm in height by wire-electrode cutting. The optical microstructure of the specimen after hot treatment is shown Fig. 1, which consists of coarse β-grains and strip α-grains. The graphite lubricant and sheets were put on the both ends of the specimen so as to reduce the friction. All hot compression tests were carried out on a Gleeble−3500 isothermal simulator at different temperatures of 1023, 1073, 1123, 1173, 1223, 1273, 1323, 1373 and 1423 K, and different strain rates of 0.01, 0.1, 1 and 10 s^{-1} with a height reduction of 60%. All specimens were resistance-heated to the deformation temperature by 10 K/s and held for 180 s to obtain a uniform temperature and decrease the material anisotropy. Finally, the specimens were quickly quenched into water to retain the elevated-temperature microstructures and sectioned perpendicular to the deformation axis for microstructure observation after being polished and corroded.

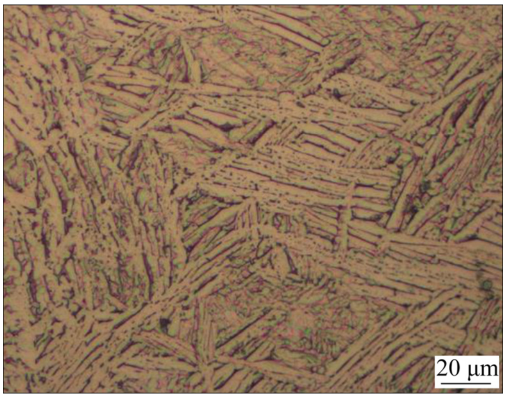

Fig. 1 Microstructure of Ti−6Al−4V−0.1Ru titanium alloy after hot treatment

During the compression processes, the nominal stress−strain relationships were continuously recorded by computer equipped with an automatic data acquisition system and then converted into true stress and true strain according to the following formula: $\sigma_T=\sigma_N(1+\varepsilon_N)$ and $\varepsilon_T=\ln(1+\varepsilon_N)$, where σ_T is true stress, σ_N is nominal stress, ε_T is true strain and ε_N is nominal strain.

3 Results and discussion

3.1 Flow behavior

The true stress−strain curves of Ti−6Al−4V−0.1Ru titanium alloy under different deformation conditions are illustrated in Fig. 2. It is shown that the flow stress is sensitively dependent on the strain rate and temperature. By comparing, the flow stress increases markedly with increasing strain rate at a given temperature and decreasing temperature at a given strain rate. For the evolution of stress with strain, it can be divided into three distinct stages [18−22]. In the first stage, the flow stress

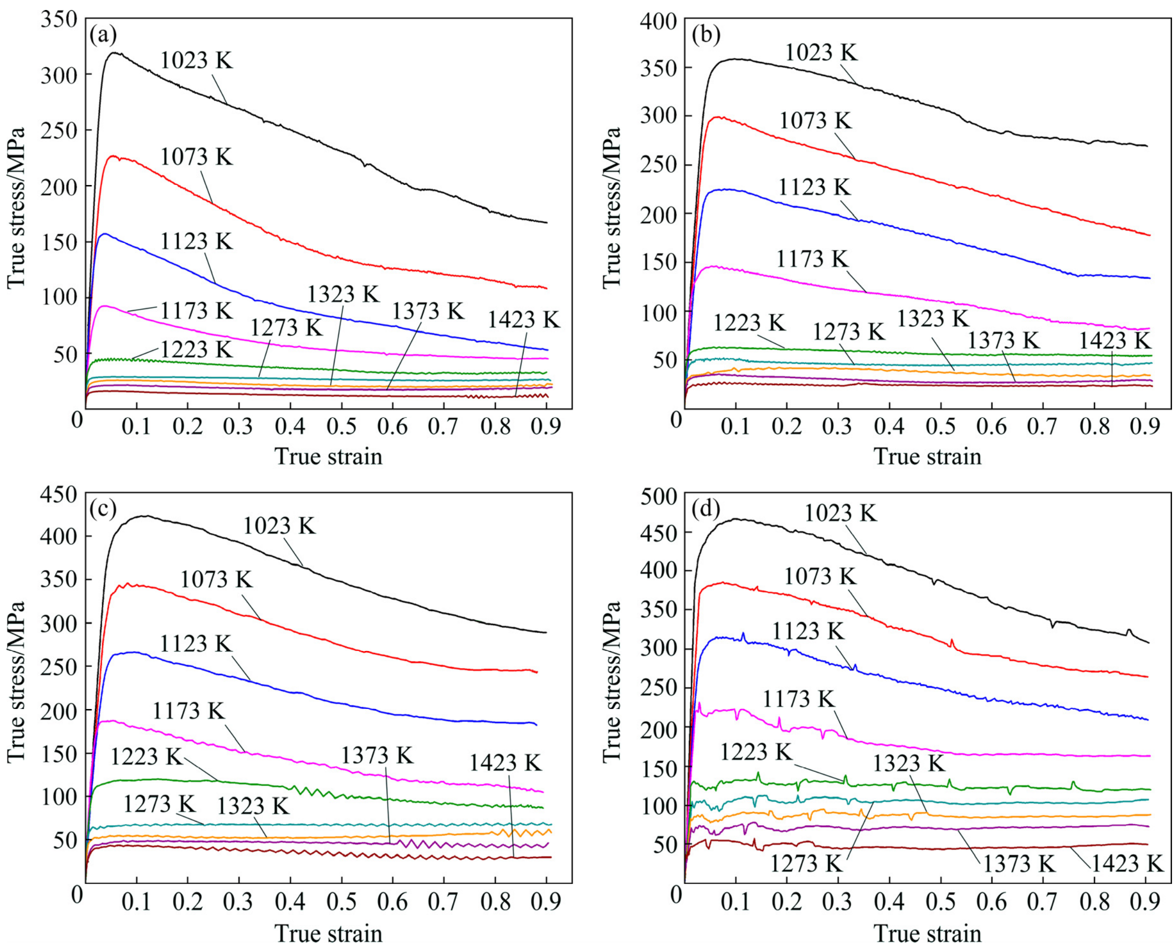

Fig. 2 True strain−stress curves of Ti−6Al−4V−0.1Ru titanium alloy at different temperatures and stain rates: (a) 0.01 s^{-1}; (b) 0.1 s^{-1}; (c) 1 s^{-1}; (d) 10 s^{-1}

increases dramatically with increasing strain, where work hardening (WH) predominates. Once the stored energy in the grain boundaries increases to a critical value, the recrystallization nucleation starts to occur, which induces dynamic softening behavior. In the second stage, flow stress slowly increases to a peak, where DRX and DRV begin to neutralize the work hardening gradually. In the third stage, the variation tendency of flow curve can be divided into two types: at 1023−1173 K in $\alpha+\beta$ phase temperature range, the flow stress continuously declines to stable value manifested by DRX softening. However, at 1023−1173 K in β phase temperature range, flow stress rapidly reaches a steady-state characteristic by DRV softening [23]. As shown in Fig. 1, α-grains dispersedly distribute on the β-grain matrix. In the initial stage of compression deformation below the β transus temperature, the grain boundaries are elongated and fractured along the flow direction of alloy, and the difference of grain boundaries gradually disappears. When corresponding critical conditions are reached, the fine spherical α grains first appear on the primary grain boundary with the occurrence of DRX, and the remaining α crystal grains without recrystallization maintain fibrous and rod-shaped. Figure 3(a) shows a typical $\alpha+\beta$ phase compressed microstructure. DRX leads to the gradual decrease of work hardening rate, following which, the flow stress gradually decreases to a stable state. When the deformation temperature is higher than β transus temperature, the emergence of cross slip and the reduction of dislocation density offset most of the work hardening. Then, the flow stress rapidly reaches a smooth steady-state characteristic, manifesting that equilibrium of WH and DRV softening. As shown in Fig. 3(b), all the α phases transform into high temperature β phase.

By comparing these curves in Fig. 2, it is found that the tendency of flow softening is more obvious at lower temperature and larger strain rate. The reason is that low temperature reduces the ability of dislocation slip and interface migration, and high strain rate increases dislocation generation rate and the number of pile-up group. Therefore, the energy accumulation time at the grain boundary becomes shorter and the mobility becomes lower, which leads to the nucleation, growth of dynamically-recrystallized grains and dislocation annihilation. Furthermore, it is interesting to note that oscillatory flow curves are observed at strain rate larger than 1 s^{-1} with increasing temperature, which exhibits a regime of flow instabilities. By observing compressed sample, the serrate oscillation phenomenon is associated with fold belt and shear cracking 45° to the direction of the compression axis due to intensive slip band formation. The surface of compressing sample even has extensive cracking, which is attributed to the secondary tensile stresses caused by bulging of the cylindrical specimen in upsetting [24,25].

3.2 Improved Arrhenius-type constitutive models

As shown in Fig. 2, it is necessary to establish corresponding constitutive models and material constants for different phases due to the difference of softening mechanism and flow stress between $\alpha+\beta$ phase and β phase regions.

3.2.1 Arrhenius-type constitutive equation

The constitutive equation of flow stress, temperature and strain rate can be well described and frequently used in Arrhenius-type model,

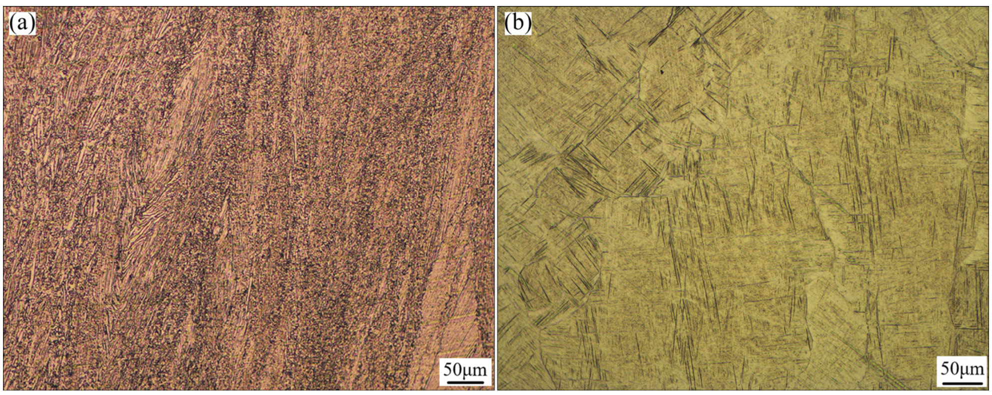

Fig. 3 Typical microstructures of Ti−6Al−4V−0.1Ru titanium alloy under different deformation conditions at strain of 0.9: (a) 1173 K, 0.01 s^{-1}; (b) 1273 K, 0.01 s^{-1}

especially at high temperatures. Moreover, the effects of temperatures and strain rate on the deformation behaviors can be represented by Zener–Hollomon parameter in an exponent-type equation. The two equations are expressed as follows:

$$\dot{\varepsilon} = AF(\sigma)\exp[-Q/(RT)] \tag{1}$$

$$Z = \dot{\varepsilon}\exp[Q/(RT)] \tag{2}$$

where $\dot{\varepsilon}$ is the strain rate (s^{-1}), σ is the stress (MPa), Q is the activity energy of hot deformation (kJ/mol), A is frequency factor, T is absolute temperature (K) and R is the universal gas constant (8.314 $J \cdot mol^{-1} \cdot K^{-1}$). The value of Q indicates the intrinsic microstructural mechanism during hot deformation.

$$F(\sigma) = \begin{cases} \sigma^{n_1}, & \alpha\sigma < 0.8 \\ \exp(\beta\sigma), & \alpha\sigma < 1.2 \\ \sinh(\alpha\sigma)^n, & \text{for all } \sigma \end{cases} \tag{3}$$

where α, β, n_1 and n are material constants, n is stress exponent (n=1/m, m is the strain rate sensitivity), and α=β/n_1. It should be pointed out that the equation only considers the effects of strain rate and temperature on flow stress. The power law and the exponential law adapt the scope of low stress level ($\alpha\sigma$<0.8) and high stress level ($\alpha\sigma$>1.2), respectively, and the hyperbolic sine type equation is suitable for all the stress level.

3.2.2 Determination of material constants

The true stress–strain data obtained through hot compression tests can be used to determine the material constants in the constitutive equation. It can be seen from Fig. 2 that the flow stress of Ti−6Al−4V−0.1Ru titanium alloy changes with the strain, which indicates that the material constants are related to the strain. In this study, take the true strain of 0.1 as an example to introduce the identification process of the material constants.

At a given deformation temperature, for the low stress level ($\alpha\sigma$<0.8) and high stress level ($\alpha\sigma$>1.2), substituting the power law and exponential law into Eq. (1), respectively, gives

$$\dot{\varepsilon} = A_1\sigma^{n_1}\exp[-Q/(RT)] \tag{4}$$

$$\dot{\varepsilon} = A_2\exp(\beta\sigma)\exp[-Q/(RT)] \tag{5}$$

where A_1 and A_2 are the material constants, and they are independent of the deformation temperature. Taking the natural logarithm on both sides of Eq. (4) and Eq. (5), and the following equations can be obtained:

$$\ln\dot{\varepsilon} = n_1\ln\sigma + \ln A_1 - Q/(RT) \tag{6}$$

$$\ln\dot{\varepsilon} = \beta\sigma + \ln A_2 - Q/(RT) \tag{7}$$

Then, the true stress values and corresponding strain rates at the strain of 0.1 are substituted into Eqs. (6) and (7). The values of n_1 and β can be obtained from the average value of the slope of $\ln\sigma - \ln\dot{\varepsilon}$ and $\sigma - \ln\dot{\varepsilon}$ plots, respectively. The mean values of n_1 and β are 5.6171 and 0.0502, and then α=β/n_1= 0.0089 MPa^{-1}.

All the stress level can be represented as follows:

$$\dot{\varepsilon} = A[\sinh(\alpha\sigma)]^n\exp[-Q/(RT)] \tag{8}$$

Taking the natural logarithm on both sides of Eq. (8) leads to

$$\ln\dot{\varepsilon} = \ln A + n\ln[\sinh(\alpha\sigma)] - Q/(RT) \tag{9}$$

The values of Q and n can be derived from the mean slopes of the $\ln[\sinh(\alpha\sigma)] - 1/T$ plots and the $\ln[\sinh(\alpha\sigma)] - \ln\dot{\varepsilon}$ plots, as illustrated in Fig. 4. Hence, by substituting the values of temperatures and true stress at the strain of 0.1 obtained from each strain rate, the value of Q and n are determined to be 682.42 kJ/mol and 4.7532 in α+β phase field and 385.45 kJ/mol and 5.1758 in β phase field, respectively. Then, the mean value of A can be obtained from the intercept of $\ln[\sinh(\alpha\sigma)] - \ln\dot{\varepsilon}$ plot, which is calculated to be 3.6152×10^{28} s^{-1} in α+β phase field and 1.0029×10^{15} s^{-1} in β phase field, respectively.

By combining Eq. (2) and Eq. (8), the constitutive equation of flow stress related to Z parameter can be written as

$$\sigma = \frac{1}{\alpha}\ln\left\{\left(\frac{Z}{A}\right)^{1/n} + \left[\left(\frac{Z}{A}\right)^{2/n} + 1\right]^{1/2}\right\} \tag{10}$$

3.2.3 Compensation of strain

In previous studies, the effect of strain on flow stress was not considered in Eq. (1). In order to establish the constitutive equation related to the continuous strain change, a series of material constants (Q, n, A and α) in Arrhenius-type model were computed at various strains in the range from 0.1 to 0.8 with an interval of 0.1, and the relationships between Q, n, $\ln A$, α and true strain for Ti−6Al−4V−0.1Ru titanium alloy can be polynomially fitted by the compensation of strain.

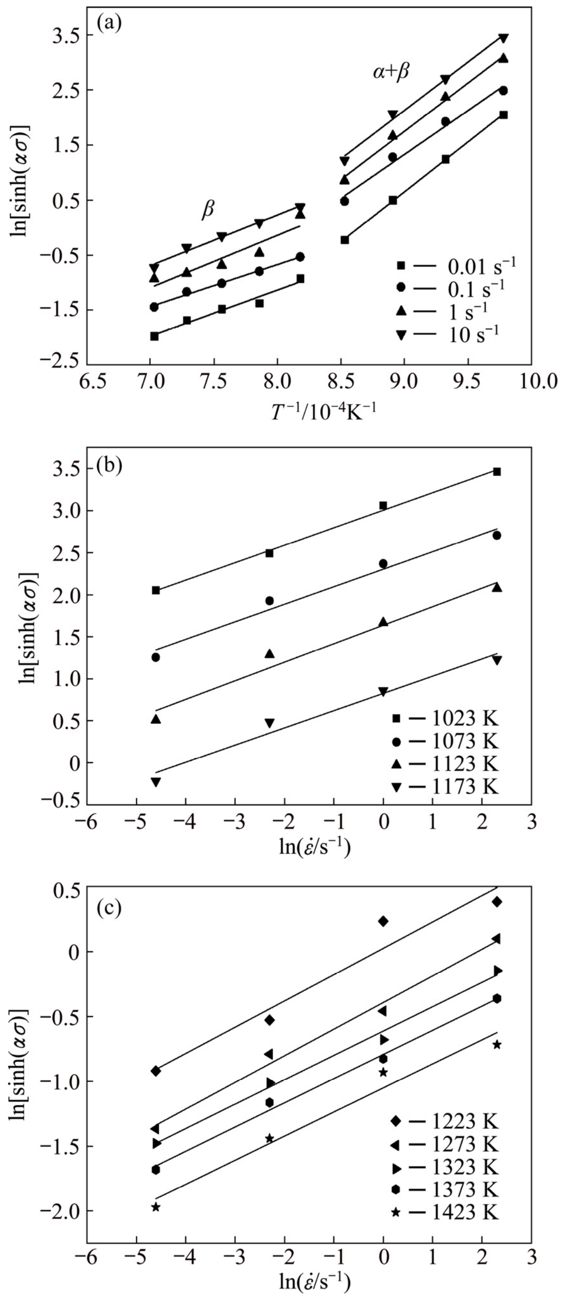

Fig. 4 Linear relationship between ln[sinh($\alpha\sigma$)] and $1/T$ (a) and between ln[sinh($\alpha\sigma$)] and $\ln\dot{\varepsilon}$ (b, c)

The fifth-degree polynomial function shown in Eq. (11) presents a good fit for the effect of true strain on the material constants [26]:

$$\begin{cases} Q = b(\varepsilon) = B_0 + B_1\varepsilon + B_2\varepsilon^2 + B_3\varepsilon^3 + B_4\varepsilon^4 + B_5\varepsilon^5 \\ n = c(\varepsilon) = C_0 + C_1\varepsilon + C_2\varepsilon^2 + C_3\varepsilon^3 + C_4\varepsilon^4 + C_5\varepsilon^5 \\ \ln A = d(\varepsilon) = D_0 + D_1\varepsilon + D_2\varepsilon^2 + D_3\varepsilon^3 + D_4\varepsilon^4 + D_5\varepsilon^5 \\ \alpha = e(\varepsilon) = E_0 + E_1\varepsilon + E_2\varepsilon^2 + E_3\varepsilon^3 + E_4\varepsilon^4 + E_5\varepsilon^5 \end{cases} \tag{11}$$

The effects of true strain on the material constants are shown in Fig. 5, and polynomial fitting results of Q, n, $\ln A$ and α of Ti−6Al−4V−0.1Ru titanium alloy are given in Table 1. Finally, substituting the polynomial functions of Q, n, $\ln A$ and α into Eq. (10) and Eq. (2), the improved Arrhenius-type constitutive models for hot deformation behaviors of Ti−6Al−4V−0.1Ru alloy are expressed as

$$\begin{cases} \sigma = \dfrac{1}{e(\varepsilon)} \ln\left\{ \left(\dfrac{Z_{[b(\varepsilon)]}}{\exp[d(\varepsilon)]} \right)^{\frac{1}{c(\varepsilon)}} + \left[\left(\dfrac{Z_{[b(\varepsilon)]}}{\exp[d(\varepsilon)]} \right)^{\frac{2}{c(\varepsilon)}} + 1 \right]^{1/2} \right\} \\ Z = \dot{\varepsilon} \exp\left[\dfrac{b(\varepsilon)}{RT} \right] \end{cases} \tag{12}$$

3.2.4 Verification of improved constitutive equation

Figure 6 shows comparisons between the experimental data and predicted values by the improved constitutive equations, and it can be seen that the predicted results relatively coincide with the experimental results at the strain softening stage. The accuracy of the equation was further evaluated by employing correlation coefficient R and the average of the absolute relative error $AARE$, as shown in Eq. (13) and Eq. (14), respectively:

$$R = \frac{\sum_{i=1}^{N} (E_i - \bar{E})(P_i - \bar{P})}{\sqrt{\sum_{i=1}^{N} (E_i - \bar{E})^2 \sum_{i=1}^{N} (P_i - \bar{P})^2}} \tag{13}$$

$$AARE = \frac{1}{N} \sum_{i=1}^{N} \left| \frac{E_i - P_i}{E_i} \right| \times 100\% \tag{14}$$

where E and P are the experimental and the predicted flow stress (MPa), respectively; $\bar{E}$ and $\bar{P}$ are the mean values of E and P, respectively; N is the number of data employed in the investigation. Figure 7 shows correlation between predicted and experimental data for the improved constitutive equation in different phase fields. The values of R and $AARE$ are found to be 0.9823 and 8.4% in $\alpha+\beta$ phase field, and 0.9753 and 9.9% in β phase field, respectively, which shows that the improved Arrhenius-type model can be used to predict the elevated-temperature flow stress behavior for Ti−6Al− 4V−0.1Ru alloy.

3.3 Relationships between *Z*-parameter maps and microstructural evolution

As a temperature-compensating strain rate factor, Zener–Hollomon parameter (Z-parameter)

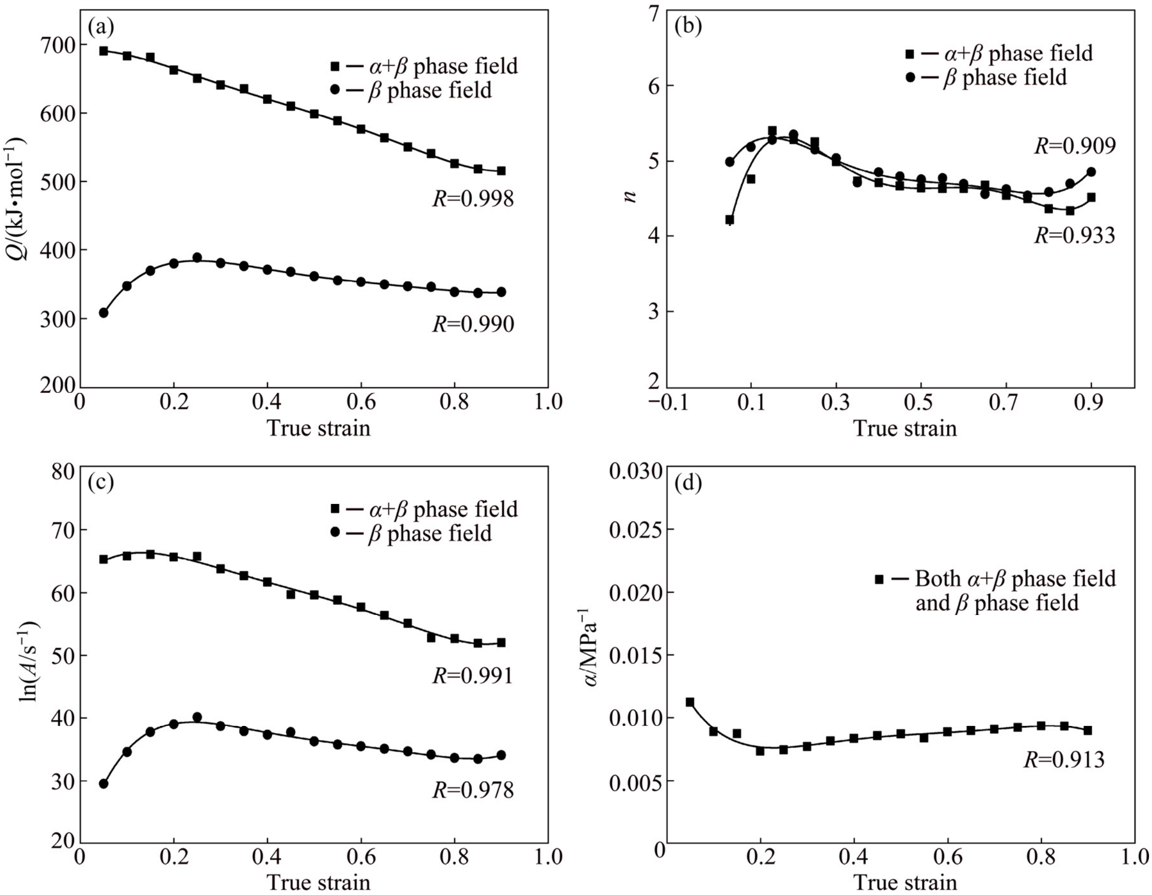

Fig. 5 Relationships between Q (a), n (b), $\ln A$ (c), and α (d) and true strain by polynomial fit

Table 1 Polynomial fitting results of Q, n, $\ln A$ and α of Ti−6Al−4V−0.1Ru titanium alloy

$\alpha+\beta$ phase				β phase			
Q	n	$\ln A$	α	Q	n	$\ln A$	α
B_0=693.86	C_0=1.789	D_0=60.877	E_0=0.015	B_0=240.7	C_0=4.215	D_0=18.364	E_0=0.015
B_1=−12.869	C_1=50.077	D_1=91.209	E_1=−0.105	B_1=1617.2	C_1=17.414	D_1=254.78	E_1=−0.105
B_2=−1310.7	C_2=−253.69	D_2=−530.24	E_2=0.491	B_2=−6684.4	C_2=−97.249	D_2=−1132.4	E_2=0.491
B_3=3808.3	C_3=559.32	D_3=1197.1	E_3=−1.019	B_3=12553	C_3=223	D_3=2277.6	E_3=−1.019
B_4=−4929.9	C_4=−565.78	D_4=−1282.1	E_4=0.989	B_4=−11382	C_4=−234.11	D_4=−2177.1	E_4=0.989
B_5=2291.3	C_5=214.53	D_5=519.95	E_5=−0.366	B_5=4019.2	C_5=92.751	D_5=798.69	E_5=−0.366

represents the combined effects of strain rate and deformation temperature on the hot deformation behavior, and has been extensively applied to investigating the microstructural evolution and hot workability of material [27−30]. Hence, the Z-parameter maps drawn at a given strain can be divided into different zones to describe the relationship between microstructure and deformation conditions.

The values of Z-parameter calculated at the true strain of 0.9 under different deformation conditions are presented in Table 2, and the corresponding Z-parameter maps for different phase fields are illustrated in Fig. 8. Apparently, the Z-parameter increases significantly with the decrease of temperature and increase of strain rate in all the phase fields. Figure 8(a) shows the microstructural evolution from flow instability to partial globularization, and finally to full globularization with equiaxed crystal for the $\alpha+\beta$ phase field. The flow localization can be observed from Fig. 9(a) when Z exceeds 1×10^{24} because the deformed specimens is exposed for a short time at the high strain rate, and thermal energy generated

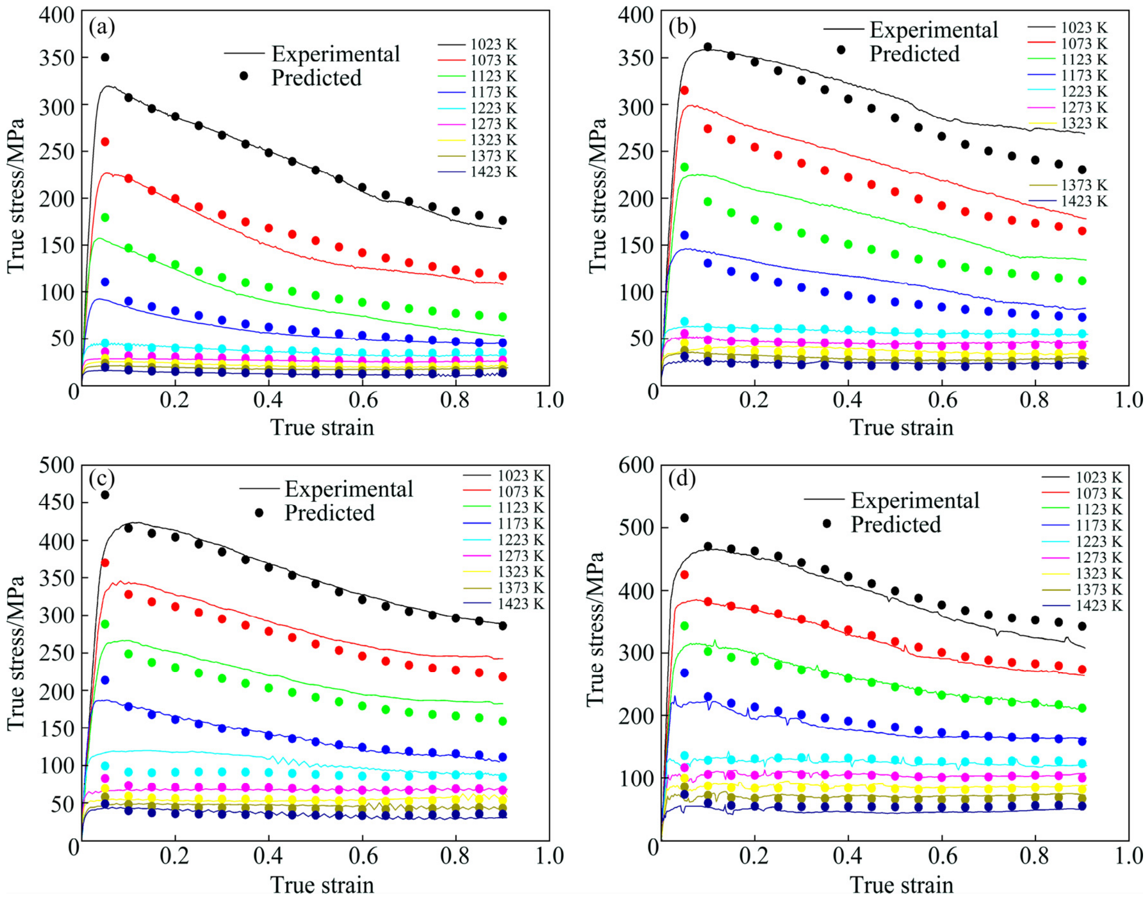

Fig. 6 Comparison between predicted and experimental flow stress curves for Ti−6Al−4V−0.1Ru titanium alloy at different strain rates: (a) 0.01 s^{-1}; (b) 0.1 s^{-1}; (c) 1 s^{-1}; (d) 10 s^{-1}

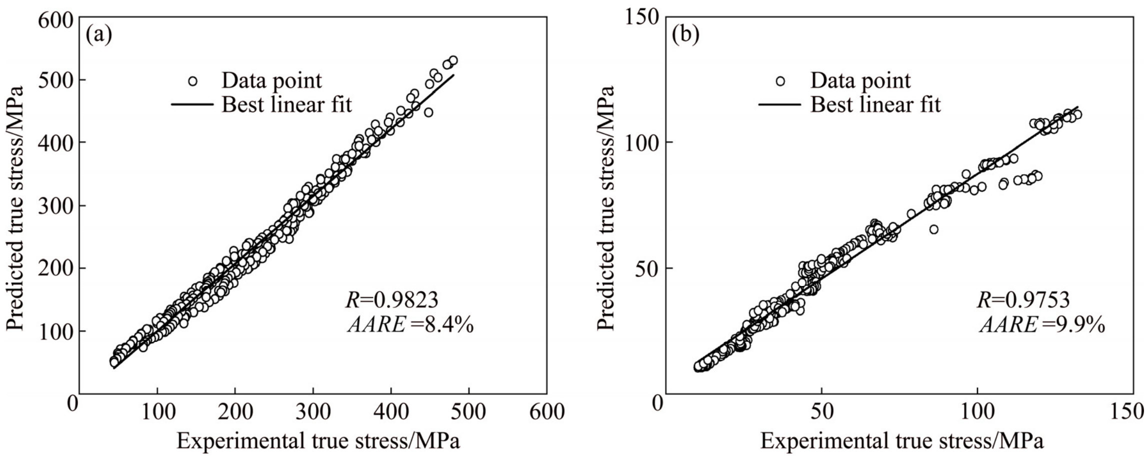

Fig. 7 Correlation between predicted and experimental data for improved constitutive equation in different phase fields: (a) $\alpha+\beta$ phase field; (b) β phase field

by deformation cannot be absorbed by the material in time which results in adiabatic shear band or flow localization at low temperature [24]. The dynamic recrystallization begins to appear when Z is in the range of 10^{22}−10^{24}, and the microstructure of the deformed specimen is completely transformed into equiaxed crystals when Z is less than 1×10^{24}, as shown in Figs. 9(b, c). In addition, the globularization process becomes violent with increasing temperature due to the activation of more dislocation slipping and climbing which makes new recrystallized grains easier to nucleate

Table 2 Values of Zener−Hollomon parameter at true strain of 0.9 under different deformation conditions

Temperature/K	Z			
	$\dot{\varepsilon}$=0.01 s^{-1}	$\dot{\varepsilon}$=0.1 s^{-1}	$\dot{\varepsilon}$=1 s^{-1}	$\dot{\varepsilon}$=10 s^{-1}
1023	1.7159×10^{24}	1.7159×10^{25}	1.7159×10^{26}	1.7159×10^{27}
1073	1.028×10^{23}	1.028×10^{24}	1.028×10^{25}	1.028×10^{26}
1123	7.9138×10^{21}	7.9138×10^{22}	7.9138×10^{23}	7.9138×10^{24}
1173	7.5805×10^{20}	7.5805×10^{21}	7.5805×10^{22}	7.5805×10^{23}
1223	2.6051×10^{12}	2.6051×10^{13}	2.6051×10^{14}	2.6051×10^{15}
1273	7.0731×10^{11}	7.0731×10^{12}	7.0731×10^{13}	7.0731×10^{14}
1323	2.1193×10^{11}	2.1193×10^{12}	2.1193×10^{13}	2.1193×10^{14}
1373	6.9326×10^{10}	6.9326×10^{11}	6.9326×10^{12}	6.9326×10^{13}
1423	2.4530×10^{10}	2.4531×10^{11}	2.4531×10^{12}	2.4531×10^{13}

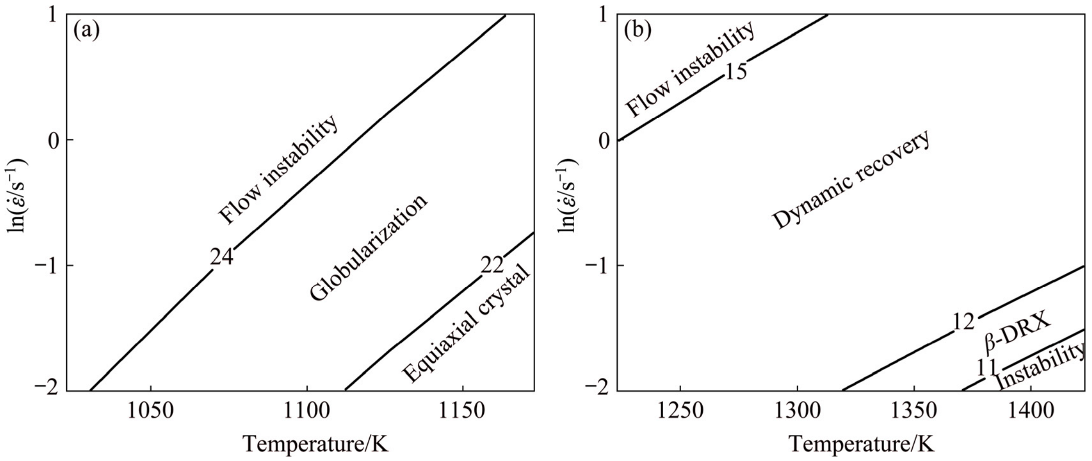

Fig. 8 Z-parameter maps of Ti−6Al−4V−0.1Ru titanium alloy under different conditions: (a) α+β phase field; (b) β phase field

at the boundaries of grains, demonstrating that equiaxed DRX occurs more easily with decreasing Z. Figure 8(b) shows the microstructural evolution from flow instability and dynamic recovery to β-DRX, and finally to instability state for the β phase field. When Z is in the range of 10^{12}−10^{15}, DRV is the main recovery mechanism, and grain boundaries of martensite grains are not clear in Fig. 10(a) which is attributed to the reason that the dislocation substructures are easily homogenized by self-diffusion of titanium atoms in sufficient time [31]. The emergence of β-DRX exhibiting in Fig. 10(b) may be caused by higher thermal activation and bcc crystal structure of β phase with increasing temperature and strain. However, the instability state of the microstructures of Ti−6Al−4V−0.1Ru titanium alloy is easily presented in the deformation condition of high temperature and high strain rate because the high strain rate can lead to the formation of adiabatic shear band or flow localization at low temperature and intergranular cracking at high temperatures [26].

3.4 Model application in isothermal compression deformation

To further evaluate the accuracy and predication performance of the improved Arrhenius-type constitutive model, the isothermal compression tests were simulated in the FEM simulation software DEFORM-2D. The flow stress data predicted by the improved Arrhenius-type models at temperatures of 1048, 1098, 1148 and 1198 K under strain rates of 0.01, 0.1, 1 and 10 s^{-1} are shown in Fig. 11. The hot compression simulations corresponding to the original billet size with a height reduction of 60% were carried out at 1073 K and 0.1 s^{-1}, and one half of the billet was used in FEM simulation due to geometric symmetry. The shear friction factor of 0.3 between the dies and surfaces of billet was chosen and thermal radiation

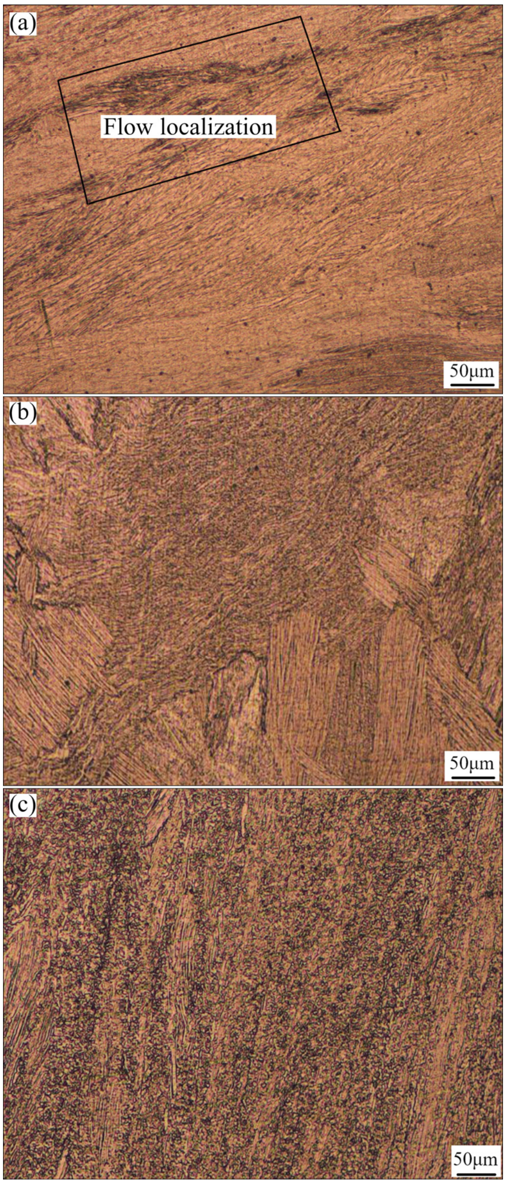

Fig. 9 Typical microstructures of Ti−6Al−4V−0.1Ru titanium alloy for α+β phase under different deformation conditions at strain of 0.9: (a) 1073 K, 1 s^{-1}, Z=1.114×10^{25}, flow localization; (b) 1073 K, 0.01 s^{-1}, Z=1.114×10^{23}, partial globularization; (c) 1123 K, 0.01 s^{-1}, Z=8.540×10^{21}, full globularization

and heat change among objects were ignored to imitate actual isothermal compression test. Besides, the bottom die was set to be fixed, and the movement of the top die was set by displacement control mode.

In the deforming simulation, all the initial conditions were identical except for the true stress−strain curves. In Scheme-1, the true stress−strain curves were obtained from hot compression tests at temperatures of 1023, 1073, 1123, 1173 K and the strain rate of 0.1 s^{-1}. However, the true stress−strain data at the temperature of 1073 K and strain rate of 0.1 s^{-1} were acquired by interpolation method in FEM software for Scheme-2. The true stress−strain curves calculated by the improved Arrhenius-type model at the temperatures of 1023, 1073, 1123, 1173 K and the strain rate of 0.1 s^{-1} were applied to Scheme-3. Meanwhile, the experimental true stress−strain curves at temperatures of 1023, 1123, 1173 K, the predicted stress−strain curves at temperatures of 1048, 1098, 1148 and 1198 K and the true stress−strain curve at the temperature of 1073 K and strain rate of 0.1 s^{-1} interpolated by FEM software were applied to Scheme-4.

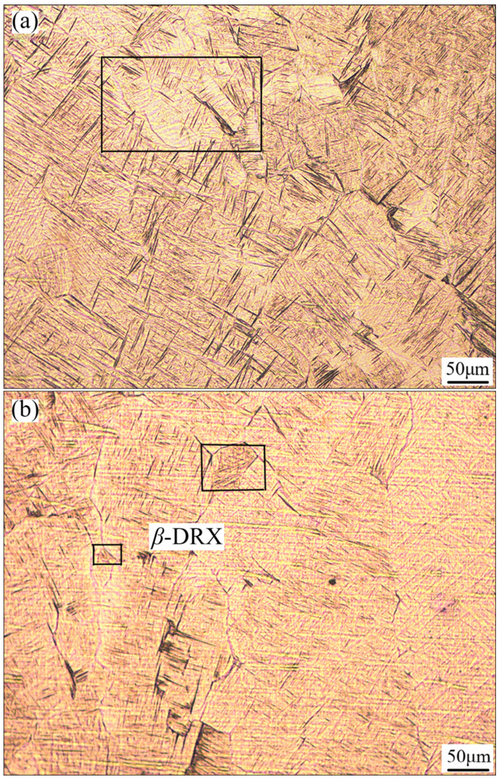

Fig. 10 Typical microstructures of Ti−6Al−4V−0.1Ru titanium alloy for β phase under different deformation conditions at strain of 0.9: (a) 1323 K, 0.01 s^{-1}, Z=4.329×10^{11}, DRV; (b) 1373 K, 0.01 s^{-1}, Z=1.380×10^{11}, β-DRX

Figure 12 shows the results of simulations expressed by strain-effective distribution maps, which can be roughly divided into three regions, and the average strains in Sheme-1, Scheme-2, Scheme-3 and Scheme-4 are 0.980, 0.917, 0.930 and 0.914, respectively. In addition, the shape of outer perimeter of the billet has the typical drum-type in each scheme. In order to quantify the

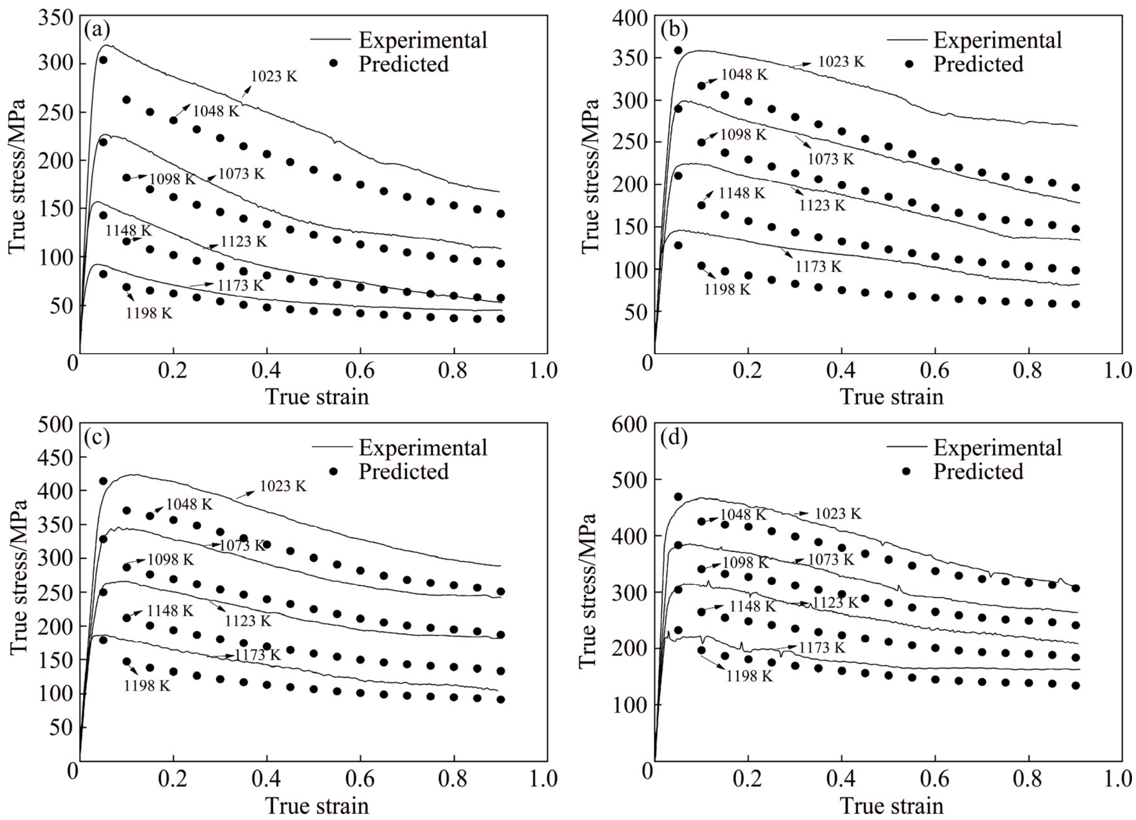

Fig. 11 True stress−strain curves of Ti−6Al−4V−0.1Ru titanium alloy under different deformation conditions: (a) 0.01 s^{-1}; (b) 0.1 s^{-1}; (c) 1 s^{-1}; (d) 10 s^{-1} (Curves at 1048, 1098, 1148 and 1198 K are predicted by improved Arrhenius-type model)

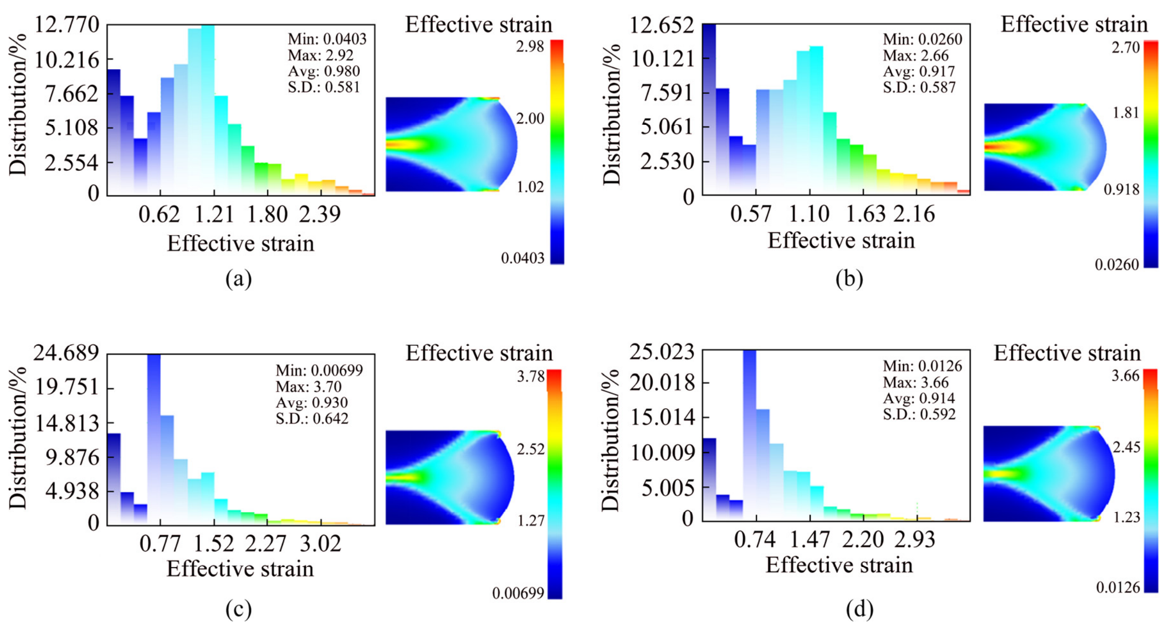

Fig. 12 Distributions of effective strain by Scheme-1 (a), Scheme-2 (b), Scheme-3 (c) and Scheme-4 (d) at strain rate of 0.1 s^{-1} and total height reduction of 60%

accuracy of each scheme, the top die load−stroke curves of four different schemes at 1073 K and 0.1 s^{-1} are exhibited in Fig. 13, which show that Scheme-2, Scheme-3 and Scheme-4 are built to predict the mechanical response of the specimen with acceptable accuracy. Moreover, the *AARE*-

value of the top die load is calculated as 7.00% between Scheme-1 and Scheme-2, 6.70% between Scheme-1 and Scheme-3, which indicates that the flow curves predicted by the improved Arrhenius-type model lead to more accurate results than interpolation method in FEM software. And it is 6.23% between Scheme-1 and Scheme-4, smaller than Scheme-1 and Scheme-2, which indicates that the small span of interpolation is more consistent with the upsetting experimental results. Consequently, it can be summarized that the improved Arrhenius-type model can be effectively used to the FEM simulation software, and predicted stress−strain data obtained by the improved Arrhenius-type model can be used to improve the simulation precision by narrowing the interpolation intervals.

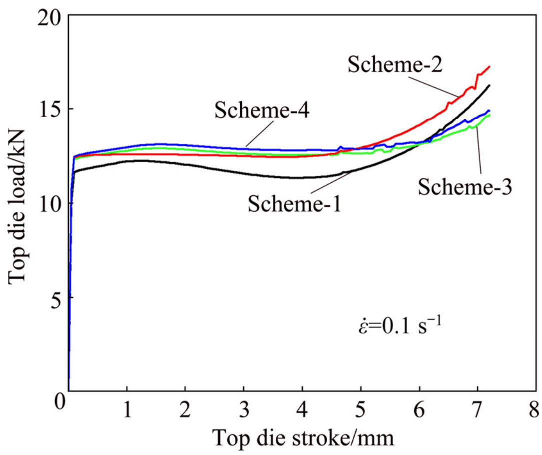

Fig. 13 Corresponding relationships between stoke and loading of top die for four schemes

4 Conclusions

(1) The predicted results obtained from the improved Arrhenius-type models relatively coincide with the experimental results at the strain softening stage.

(2) Based on the Z-parameter maps and microstructural analysis, in $\alpha+\beta$ dual phase field, it can be concluded that the globularization is more likely to occur with the Z less than 1×10^{24}. When the value of Z-parameter is lower, the flow stress is lower and the globularization may occur more easily. The microstructural evolution of Ti−6Al−4V−0.1Ru titanium alloy transforms from flow instability and dynamic recovery to β-DRX, and finally to instability state for β single phase field. By combining the microstructure observation with Z-parameter maps, the hot working process of Ti−6Al−4V−0.1Ru titanium alloy can be adjusted to obtain expected final microstructure.

(3) The simulation results indicate that the improved Arrhenius-type model is an effective and promising tool to simulate the upsetting process, and stress−strain data calculated by the improved Arrhenius-type model can be used to reduce the interpolation intervals, which can obtain more accurate simulation results.

References

[1] SCHUTZ R W, WATKINS H B. Recent developments in titanium alloy application in the energy industry [J]. Materials Science and Engineering A, 1998, 243: 305−315.

[2] STUART R S, MORTEN A L. Fatigue-crack growth in Ti−6Al−4V−0.1Ru in air and seawater: Part I. Design of experiments, assessment, and crack-growth-rate curves [J]. Metallurgical and Materials Transactions A, 2001, 32(9): 2297−2314.

[3] LIN Y C, CHEN X M. A critical review of experimental results and constitutive descriptions for metals and alloys in hot working [J]. Materials and Design, 2011, 32(4): 1733−1759.

[4] LIN Y C, HE M, ZHOU M, WEN D X, CHEN J. New constitutive model for hot deformation behaviors of Ni-based superalloy considering the effects of initial δ phase [J]. Journal of Materials Engineering and Performance, 2015, 24(9): 3527−3538.

[5] LIN Y C, CHEN M S, ZHONG J. Prediction of 42CrMo steel flow stress at high temperature and strain rate [J]. Mechanics Research Communications, 2008, 35(3): 142−150.

[6] TABEI A, ABED F H, VOYIADJIS G Z, GARMESTANI H. Constitutive modeling of Ti−6Al−4V at a wide range of temperatures and strain rates [J]. European Journal of Mechanics A: Solids, 2017, 63: 128−135.

[7] HIROAKI M, VINCENT V. Mesoscale modeling of dynamic recrystallization behavior, grain size evolution, dislocation density, processing map characteristic, and room temperature strength of Ti−6Al−4V alloy forged in the ($\alpha+\beta$) region [J]. Journal of Alloys and Compounds, 2017, 708: 404−413.

[8] SCHUTZ R W. Ruthenium enhanced titanium alloys: Minor ruthenium additions produce cost effective corrosion resistant commercial titanium alloys [J]. Platinum Metals Review, 1996, 40(2): 54−61.

[9] SCHUTZ R W, HORRIGAN J M, BEDNAROWICZ T A. Stress corrosion behavior of Ru-enhanced a Lpha−Beta titanium alloys in methanol solutions [J]. NACE International, 1998, 261: 22−27.

[10] ZHAO J W, DING H, ZHAO W J, HUANG M L, WEI D B, JIANG Z Y. Modelling of the hot deformation behaviors of a titanium alloy using constitutive equations and artificial neural network [J]. Computational Materials Science, 2014, 92: 47−56.

[11] LIN Y C, WEN D X, CHEN X M, CHEN X W. A unified physically-based constitutive model for describing strain hardening effect and dynamic recovery behavior of a Ni-based superalloy [J]. Journal of Materials Research, 2015,

30(27): 3784−3794.

[12] PENG W W, ZENG W D, WANG Q J, YU H Q. Comparative study on constitutive relationship of as-cast Ti60 titanium alloy during hot deformation based on Arrhenius-type and artificial neural network models [J]. Materials and Design, 2013, 51: 95−104.

[13] MANDAL S, RAKESH V, SIVAPRASAD P V, VENUGOPAL S, KASIVISWANATHAN K V. Constitutive equations to predict high temperature flow stress in a Ti-modified austenitic stainless steel [J]. Materials Science and Engineering A, 2009, 500: 114−121.

[14] QUAN G Z, SHI Y, YU C T, ZHOU J. The improved Arrhenius model with variable parameters of flow behavior characterizing for the as-cast AZ80 magnesium alloy [J]. Materials Research, 2013, 16(4): 785−791.

[15] WU H, WEN S P, HUANG H, WU X L, GAO K Y, WANG W, NIE Z R. Hot deformation behavior and constitutive equation of a new type Al−Zn−Mg−Er−Zr alloy during isothermal compression [J]. Materials Science and Engineering A, 2016, 651: 415−424.

[16] QUAN G Z, TONG Y, LUO G, ZHOU J. A characterization for the flow behavior of 42CrMo steel [J]. Computational Materials Science, 2010, 50: 167−171.

[17] XIAO J, LI D S, LI X Q, DENG T S. Constitutive modeling and microstructure change of Ti−6Al−4V during the hot tensile deformation [J]. Journal of Alloys and Compounds, 2012, 541: 346−352.

[18] DEHGHAN-MANSHADI A, BARNETT M R, HODGSON P D. Recrystallization in AISI 304 austenitic stainless steel during and after hot deformation [J]. Materials Science and Engineering A, 2008, 485: 664−672.

[19] KIM S I, YOO Y C. Dynamic recrystallization behavior of AISI 304 stainless steel [J]. Materials Science and Engineering A, 2001, 311: 108−113.

[20] UEKI M, HORIE S, NAKAMURA T. Critical condition for transition from multiple to single peak dynamic recrystallizations [J]. Scripta Metallurgica, 1985, 19: 547−549.

[21] POLIAK E I, JONAS J J. A one-parameter approach to determining the critical conditions for the initiation of dynamic recrystallization [J]. Acta Materialia, 1996, 44: 127−136.

[22] RYAN N D, MCQUEEN H J. Flow-stress, dynamic restoration, strain-hardening and ductility in hot-working of 316-steel [J]. Journal of Materials Processing Technology, 1990, 21: 177−199.

[23] QUAN G Z, LUO G C, LIANG J T, WU D S, MAO A, LIU Q. Modelling for the dynamic recrystallization evolution of Ti−6Al−4V alloy in two-phase temperature range and a wide strain rate range [J]. Computational Material Science, 2014, 97: 136−147.

[24] ZENG W D, SHU Y, ZHANG X M, ZHOU Y G, ZHAO Y Q, WU H, DAI Y, YANG J, ZHOU L. Hot workability and microstructure evolution of highly β stabilised Ti−25V−15Cr−03Si Alloy [J]. Materials Science and Technology, 2008, 24(10): 1222−1229.

[25] SESHACHARYULU T, MEDEIROS S C, FRAZIER W G, PRASAD Y V R K. Hot working of commercial Ti−6Al−4V with an equiaxed α−β microstructure: Materials modeling considerations[J]. Materials Science and Engineering A, 2000, 284: 184−194.

[26] CAO Y, DI H S, MISRA R D K, YI X, ZHANG J C, MA T J. On the hot deformation behavior of AISI 420 stainless steel based on constitutive analysis and CSL model [J]. Materials Science and Engineering A, 2014, 593: 111−119.

[27] ZENER C, HOLLOMON J H. Effect of strain rate upon plastic flow of steel [J]. Journal of Applied Physics, 1994, 15: 22−27.

[28] CHEN X H, FEN A H, HU Z Y, YANG J J, GAO W L. Flow stress and dynamic behavior of Al−9Mg−1.1Li−0.5Mn alloy during hot compression process [J]. Transactions of Nonferrous Metals Society of China, 2018, 28: 2401−2409.

[29] ZOU D N, HAN Y, YA D N, WANG D, ZHANG W, FAN G W. Hot workability of 00Cr13Ni5Mo2 supermartensitic stainless steel [J]. Materials and Design, 2011, 32: 4443−4448.

[30] ZHANG J Q, DI H S, WANG H T, KUN M, MA T J, CAO Y. Hot deformation behavior of Ti-15-3 titanium alloy: A study using processing maps, activation energy map, and Zener–Hollomon parameter map [J]. Journal of Materials Science, 2012, 47: 4000−4011.

[1] JIA W J, ZENG W D, LIU J R, ZHOU Y G, WANG Q J. On the influence of processing parameters on microstructural evolution of a near alpha titanium alloy [J]. Materials Science and Engineering A, 2011, 530: 135−143.

等温压缩过程中 Ti−6Al−4V−0.1Ru 合金的热变形行为

夏玉峰，蒋 伟，程 千，姜 来，金 力

重庆大学 材料科学与工程学院，重庆 400044

摘 要：采用 Gleeble−3500 热模拟器对 Ti−6Al−4V−0.1Ru 合金进行等温压缩试验，研究该合金在变形温度为 1023−1423 K 和应变速率为 0.01−10 s^{-1} 条件下的热变形行为。建立应变量为 0.1 时 $\alpha+\beta$ 双相和 β 单相温度场的 Arrhenius-type 本构模型；然后，将一系列材料常数(包括激活能 Q、材料常数 n，α 和 $\ln A$)作为应变的多项式函数引入 Arrhenius-type 模型；最后，分别对 $\alpha+\beta$ 双相和 β 单相温度场构建改进的 Arrhenius-type 模型。结果表明，改进的 Arrhenius-type 模型有助于计算 Zener−Hollomon(Z)参数，通过显微观察并结合 Z 参数可以揭示显微组织演变机制；此外，该模型也有助于提高 Ti−6Al−4V−0.1Ru 钛合金变形过程中有限元模拟的精度。

关键词：Ti−6Al−4V−0.1Ru 钛合金；Arrhenius-type 本构模型；Zener−Hollomon 参数；显微组织演化；FEM 模拟

(Edited by Bing YANG)